

in places,
basal ablation of the ~~ice shelf~~ (PIIS)

Abstract

Observations beneath Pine Island Glacier (PIG) have revealed the presence of a seabed ridge, which rises several hundred metres above the surrounding bathymetry. It is understood that this ridge, in combination with the ice draft above it, form a topographic barrier, restricting access of warm Circumpolar Deep Water to a cavity inshore of the ridge, and thus exerting an important control on melt rates. In addition, Pine Island Ice Shelf (PIIS) has experienced several large calving events in recent years, and it has been suggested that further calving events that significantly reduce the size of the ice shelf are inevitable. Here, we address the question of how these two important characteristics of PIG interact: have recent, and may future, calving events of PIIS lead to a relaxation of the topographic barrier and thus significantly change melt rates? We use a high-resolution ocean model to simulate melt rates in both an idealized domain whose geometry captures the essential features of PIG, and a realistic geometry that accurately resembles it to explore how changing the ice front position (i.e. calving) affects melt rates. The idealized simulations reveal that the melt response to calving has a sensitive dependence on the cavity geometry with melt rates varying significantly with calving for narrow (≤ 150 m) ridge draft gaps, but only weakly for larger (> 150 m) ridge draft gaps. The idealized simulations inform our interpretation of the realistic simulations, which suggest that the melt rates under PIIS have not changed significantly in dynamically important regions of the ice shelf in response to recent calving, providing negative feedback on ice shelf mass loss, but large changes and positive feedback are possible if future calving when the ice shelf reaches the seabed ridge.

*could significantly
alter the cavity
geometry.*

*changes in
calving
front
location
in combination
with changes in
ice thickness
might lead
to a relaxation*

1 Introduction

Pine Island Glacier (PIG), located in the Amundsen Sea sector of Antarctica, is one of the fastest changing glaciers worldwide. A sustained increase in ice discharge and surface velocity, as well as significant grounding line retreat, have been documented since satellite measurements began in the 1990s (Rignot et al., 2002; Rignot, 2008; Rignot et al., 2011; Mouginot et al., 2014; Gardner et al., 2018). PIG has experienced a 70% increase in ice flux and a close to doubling of surface velocity between 1974 and 2013 (Mouginot et al., 2014), while its grounding line retreated some 31 km at its centre between 1992 and 2011 (Rignot et al., 2014). Increased basal melting of Pine Island Ice Shelf (PIIS) – the floating extension of the grounded ice – has been implicated as a key driver of these changes (Shepherd et al., 2004; Pritchard et al., 2012; Rignot et al., 2019): ice shelves offer a resistive stress (commonly referred to as ‘buttressing’) that restrains the flow of grounded ice; increased basal melting reduces ice shelf volume and thus the buttressing they are able to provide (Gudmundsson, 2013; Reese et al., 2018; Gudmundsson et al., 2019; Gagliardini et al., 2010; Goldberg et al., 2019; De Rydt et al., 2021).

The main source of heat for ice shelf melting in the Amundsen Sea off West Antarctica is Circumpolar Deep Water (CDW). In the Amundsen Sea, the pycnocline that separates these two water masses remains mostly above the level of the continental shelf break (Jacobs et al., 2015; Heywood et al., 2016), allowing CDW to spill onto the continental shelf and reach ice shelf cavities. This provides ice shelf cavities with significant heat to melt the adjacent ice shelves. Very roughly, the volume of CDW that is able to spill over the continental shelf sets the depth of the pycnocline. The volume of CDW that spills over the shelf, and thus the depth of the pycnocline is not constant, but varies significantly on decadal timescales (Jenkins et al., 2018). Years with a deeper pycnocline tend to result in lower meltwater fluxes from ice shelves, and vice versa (some references here)

For Pine Island specifically, this simple ‘pycnocline depth’ picture is complicated by the presence of a seabed ridge in the ice shelf cavity. This ridge is located several tens of kilometers downstream of the grounding line, and protrudes up to three hundred meters above the neighboring seabed (figure 1a). In combination with the ice shelf directly

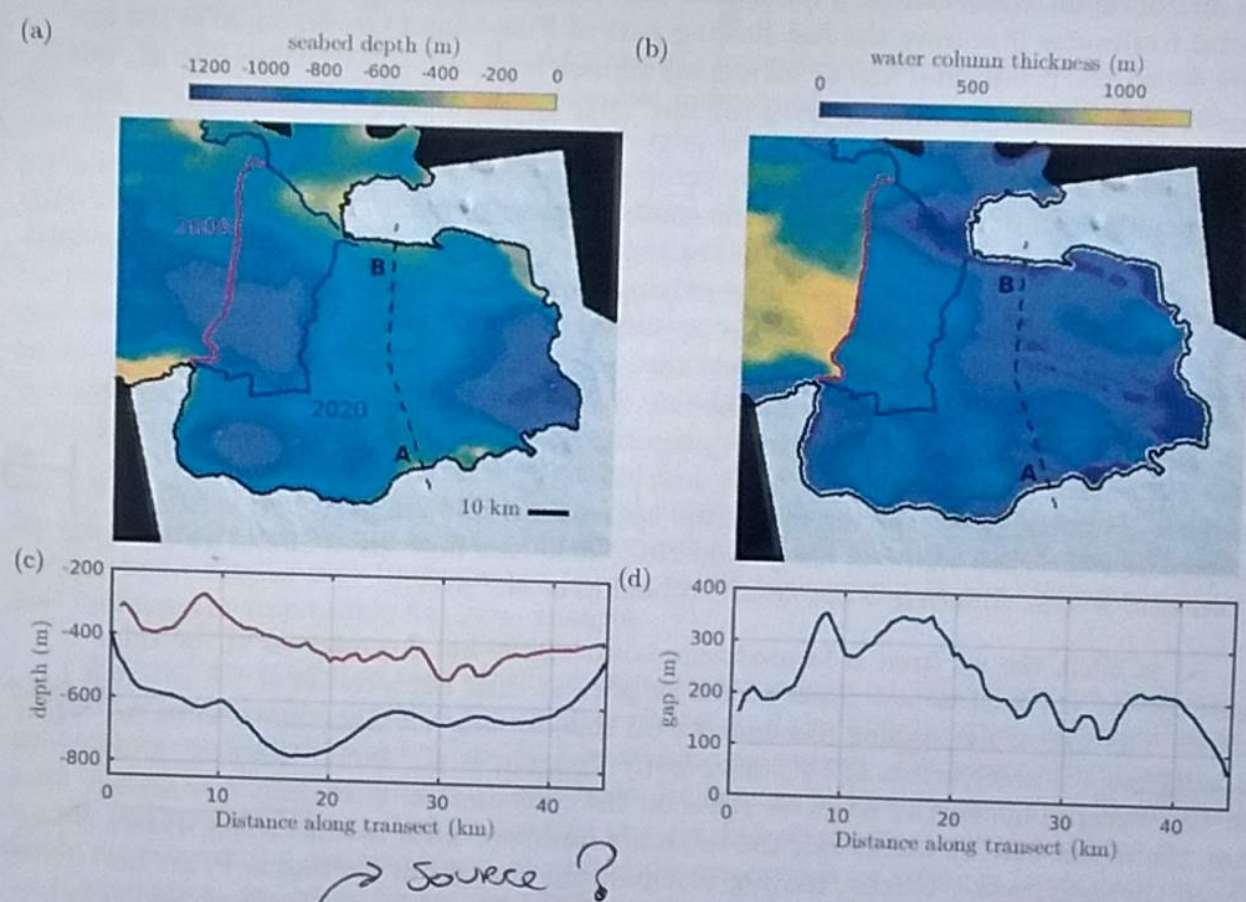


Figure 1. (a) Seabed depth and (b) water column thickness under Pine Island Ice Shelf and in Pine Island Bay (colours) alongside the location of the ice front in 2009 (red line) and 2020 (blue line), as indicated in (a). The solid black line indicates the grounding line from Jougin et al. (2010), and the background image is a Sentinel 2 mosaic from November 2020. The black dashed line indicates the approximate location of the crest of the seabed ridge. The magenta contour in (b) corresponds to 125 m water column thickness. (c) Seabed bathymetry (blue) and ice draft (red) taken along the dashed line in (a)–(b). (d) Plot of the ridge-seabed gap measured along the dashed black line in (a) (i.e. the difference between the red and blue lines in (c)).

above it, the ridge acts as a topographic barrier that restricts the access of CDW to an inner cavity that has formed between the ridge and the grounding line, since the ice shelf grounding line likely retreated from this ridge in a process initiated in the late 1940s (Jenkins et al., 2010; De Rydt et al., 2014; De Rydt & Gudmundsson, 2016; Smith et al., 2017). This cavity geometry means that the strength of the topographic barrier (i.e. how much its presence affects sub-shelf melting) is strongly dependent on the pycnocline depth: at its shallowest, the pycnocline sits above the depth of the ridge crest, and a large amount of modified CDW is able to spill into the inner cavity (Dutrieux et al., 2014); in contrast, at its lowest, the pycnocline sits some way below the ridge crest and CDW access is severely restricted. As a result, melting of ~~Pine Island Glacier~~ has a particularly strong sensitivity to hydrographic conditions in Pine Island Bay: Dutrieux et al. (2014) reported that the total freshwater flux from the fast flowing part of Pine Island Glacier in 2009 ($80 \text{ km}^3 \text{ year}^{-1}$), when the pycnocline was at its second-highest level on record (Webber et al., 2017), was more than double its value in 2012 ($37 \text{ km}^3 \text{ year}^{-1}$), when the pycnocline was at the second-lowest recorded depth.

In addition to its unique topographic control on melt rates, the recent calving of PIIS also stands out amongst Amundsen Sea terminating ice shelves. Mass losses from ice sheets in Antarctica are dominated by calving and melting (Rignot et al., 2013); in equilibrium, these losses must balance the upstream accumulation of ice. The recent retreat of ~~ice front of PIIS~~, however, suggests that the calving rate is far higher than would be required to maintain an equilibrium: the ice front retreated approximately 26 km between 2009 and 2020 (figure 1a), with the majority of this retreat happening over the period 2015–2020 (Lhermitte et al., 2020; Joughin et al., 2021). This corresponds to a more-than-doubling of the calving rate, from approximately 4 km year^{-1} prior to 2015 to approximately 9 km year^{-1} in the period 2015–2020 (the flow speed at the ice front, for context, is approximately 5 km year^{-1} (Joughin et al., 2021)).

As of 2020, the ice front is located approximately 20 km downstream of the ridge (figure 1); the ice front is now closer to the ridge crest than the location of the ice front in 2009. The loss of buttressing associated with ~~this calving has been shown to be responsible for~~ the acceleration of PIG since 2015 (Joughin et al., 2021). However, given that the topographic barrier to CDW relies on the combination of ~~ice draft and seabed ridge~~, the recent calving events beg the following question: have recent calving events relaxed the topographic barrier, leading to significant changes in melting in PIIS? Increased melting of ice shelves ~~will~~ lead to further reductions in ice shelf volume and thus buttressing, ultimately leading to ice shelf acceleration, thinning and grounding line retreat.

In addition to considering the effect on melt rates of calving events that have already happened, we also consider how melt rates might respond to possible future calving events. It has been suggested that further significant calving of PIIS is inevitable: damage to the ice shelf that has already occurred is thought to have preconditioned PIIS to collapse (Lhermitte et al., 2020). Additionally, there is a theoretical feedback loop in which damage leads to calving, reducing buttressing, leading to acceleration of the ice and (thus) further damage. We expect further calving as part of this feedback process that also interacts with unbalanced melting. The second question we aim to answer regards the melt response to calving in the future: how will melt rates on PIIS respond to possible future calving events?

In this study, we use numerical simulations in both an idealized ~~domain~~ whose geometry captures the essential features of PIG, and a realistic ~~geometry~~ that closely matches real world conditions for PIG to assess how, and why, melt rates in PIIS will respond to past and potential future calving events. We begin in §2 with a description of the experiments using the idealized geometry, setting out details of the ocean model used and the experimental setup. We perform a total of nine idealized experiments; results of one such experiment (the ‘baseline’) are presented in §3: we describe how and why the melt

} of course, etc
for a flat
bathymetry there
would be significant
var. in MR for
varying pycnocline
depth.

| Is it sensible to

retreat of the ice front
explain

needs to be
explained first.

repeat

Wgcm to simulate ab setup

say which features

rate responds to calving in this experiment. In the following two sections, we discuss how the picture presented in §3 changes for different cavity geometries (§4) and hydrographic forcings (§5). In §6, we describe and present results from the realistic experiments. Guided by the results of the idealized experiments, we assess the expected response of melt rates under PIIS to calving events. In §7, we discuss the implications of our results and summarize the key results in §8.

2 Idealized Experiment Details

In this section, we describe the setup of the experiments performed in an idealized domain whose geometry captures the essential features of the cavity under PIIS (most notably, the presence of a seabed ridge). We refer to these experiments as ‘idealized experiments’. In this idealized geometry, the gap between the ice draft and the seabed ridge (the ‘ridge-draft’ gap) is uniform in the zonal direction. In practice, however, the ridge-draft gap is non-uniform (figure 1c–d); to capture the effect of this variation, we consider the melt response to calving for several different ridge-draft gaps. We also consider several different far-field ocean conditions (‘hydrographic forcings’): as discussed in §1, melt rates of PIIS have a sensitive dependence on the hydrographic forcing via the depth of the pycnocline; we therefore expect that the melt response to calving might similarly have a sensitive dependence on the hydrographic forcing, and investigate this effect.

The benefit of considering first idealized experiments is that, by simplifying the cavity geometry, we are able to isolate the important roles that the ridge-draft gap and the hydrographic forcing play in the melt response to calving, as well as elucidating the physical mechanisms responsible for these changes.

We perform a total of nine idealized experiments, each corresponding to a unique pair of parameters that describe the ridge-draft gap and the hydrographic forcing; these parameters are described in sections §2.2 and §2.3, respectively. Each experiment consists of a series of ten simulations in which the ice front position is systematically ~~fixed~~; we use the term calving as a proxy for this process, but stress that our simulations include neither calving dynamics nor associated processes such as mélange formation. In each simulation, we explicitly ~~solve the 3D~~ ^{3D} ocean circulation using the MIT general circulation model (MITgcm) (Marshall et al., 1997). Other than removing sections of the ice shelf, the ice shelf geometry does not change ~~between~~ ^{between} experiments. Ice shelves themselves enter the ocean model passively, via the exchange of heat and salt at the ice-ocean interface and a steady pressure loading on the ocean surface (i.e. there are no ice-dynamics considerations in the cavity geometry); a passive description of ice shelves is sufficient to assess the response of melt rates to ice shelf calving, which occurs on a timescale much shorter than that on which the ice responds dynamically to perturbations in melting. In the following sections, we provide further details of the ocean model and experimental setup, including the motivation for our choices of parameters.

2.1 Details of Ocean Model

The MITgcm is a z-level general circulation model that includes a partial-cell treatment of topography, allowing an accurate description of both the seabed and ice draft. Our model grid consists of 110 layers with a vertical spacing of 10 m, and a horizontal resolution of 400 m. We use the MITgcm in hydrostatic mode with an implicit nonlinear free surface scheme, a third-order direct space-time flux limited advection scheme, and a non-linear equation of state (McDougall et al., 2003). The Pacanowski-Philander (Pacanowski & Philander, 1981) scheme parametrizes vertical mixing. Constant values of 15 and $2.5 \text{ m}^2 \text{ s}^{-1}$ are used for the horizontal Laplacian viscosity and horizontal diffusivity, respectively. The equations are solved on an *f*-plane with $f = -1.4 \times 10^{-4} \text{ s}^{-1}$.

say that
you solve
for a semi-steady
circulation, and
associated basal
melt rates for
each geometry

widths of the

) refer to Fig 2

shifted towards
the (fixed) GL?

159 Each simulation is run for twelve months using a timestep of 30 seconds, after which
 160 time the configuration is approximately in steady state. The melt rates are within 95%
 161 of their final values after three months. All results presented here are averaged over the
 162 final two months of the simulations.

~~Impact on the ocean state~~

! Ok As mentioned, ice shelves enter the simulations via the exchange of heat and salt
 at the ice-ocean interface. This exchange is implemented using the so-called "three-equation
 formulation" (Holland & Jenkins, 1999), whose implementation in MITgcm has been de-
 scribed in detail elsewhere (Losch, 2008; De Rydt et al., 2014; Dansereau et al., 2014,
 for example). Note that the temperature difference between ice shelves and the adjacent
 ocean boundary layer is ~~is~~ to two orders of magnitude smaller than the temperature
 associated with phase changes ($L/c \approx -84^\circ\text{C}$, where $L = 3.35 \times 10^5$ is the latent heat
 of fusion, and $c_p = 3947 \text{ J kg}^{-1}$ is the specific heat capacity of water). Thus, thermal
 exchange across the ice-ocean interface is typically dominated by latent heat (over heat
 conduction into the ice). With latent heat dominated thermal exchange, the three equa-
 tion formulation simplifies to give the melt rate \dot{m} as

$$\dot{m} = \frac{c_p \gamma_T (T - T_b)}{L} \quad (1)$$

Here T is the temperature far outside the viscous boundary layer that forms at the ice-
 ocean interface, T_b is the temperature at the ice shelf base, which must be at the local
 (depth and salinity dependent) freezing point, and γ_T is a heat exchange co-efficient that
 parametrizes exchange across this boundary layer. The heat exchange-coefficient γ_T has
 a weakly non-linear relationship on u^* , the ocean speed adjacent to the ice shelf base (Holland
 & Jenkins, 1999). If this relationship were perfectly linear, $\gamma_T \propto u^*$, equation (2) would
 read

$$\dot{m} \propto u^*(T - T_b). \quad (2)$$

We shall return to equation (2) when describing the mechanisms responsible for the melt
 rate response to ice shelf calving.

We use parameter values from Holland and Jenkins (1999) in the three equation
 formulation, with the exception of the drag co-efficient, which is set to 4.5×10^{-3} , a value
 that is more appropriate for Pine Island Glacier (see §6). (Note that the drag coefficient
 that enters the momentum balance, which can be set independently, remains at the stan-
 dard value of 2.5×10^{-3} .)

2.2 Ice Shelf Geometry and Seabed Bathymetry

Our idealized setup is shown schematically in figure 2a: it is uniform in the zonal
 direction, along which the x -axis is aligned, and the y -axis is aligned along the merid-
 ional direction. Note that although PIG is aligned approximately east-west, we assume
 here that it is aligned north-south, as is standard (Grosfeld et al., 1997; De Rydt et al.,
 2014). (results are independent of this choice of orientation)

The sea bed has a Gaussian profile,

$$b(x, y) = -1100 + 400 \exp \left[-\frac{(y - 50 \times 10^3)^2}{2\sigma^2} \right], \quad (3)$$

where $\sigma = 12 \text{ km}$ is the length scale over which this profile decays towards zero. The
 profile (3) corresponds to a ridge that peaks at a height of 400 m above the surround-
 ing bathymetry. This peak occurs 50 km from the southern end of the domain, which
 we consider to be the grounding line. Note that we prevent the cavity thickness from reach-
 ing zero at this grounding line as the MITgcm requires at least two grid cells in the ver-
 tical to permit horizontal transfer.

In reality, the variability in both PIIS draft and the height of the seabed ridge result in a ridge-
 draft gap that varies between approximately 100 m at its narrowest to greater than 300 m

might be
 better after you
 introduced the
 ice draft.

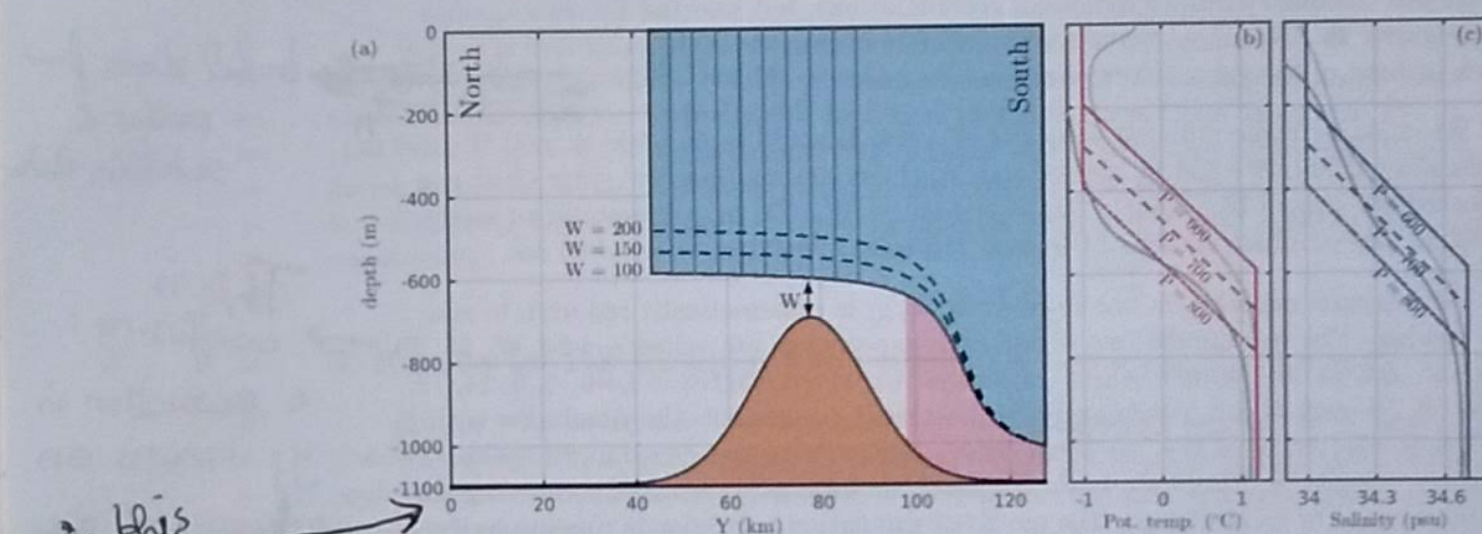


Figure 2. (a) Schematic diagram of the experimental setup. The domain is uniform in the zonal direction (into the page), with extent 48 km. The ocean domain consists of the gridded area, which is bordered by a passive ice shelf (shaded blue) and a seabed ridge (shaded brown). Solid, dashed and dot-dashed black curves indicate the location of the ice shelf base for $W=100$ m, $W=150$ m, and $W=200$ m, respectively (as labelled). Solid blue lines indicate the series of ice front positions considered within each ‘calving’ experiment, located at 80, 75, 70, 65, 60, 55, 50, 45, and 40 km offshore of the southern end of the domain. The shaded red region indicates the inner cavity, defined as areas within 30 km of the southern end of the domain. (b) Temperature and (c) salinity profiles used in the experiments. Different line styles correspond to different values of the pycnocline depth P as follows: $P=600$ m (solid), $P=700$ m (dashed), $P=800$ m (dot-dashed). Light and dark gray lines correspond to temperature and salinity profiles taken from conductivity, temperature, and depth measurements in Pine Island Bay during the austral summers of 2009 (Jacobs et al., 2011) and 2012 (Dutrieux et al., 2014), respectively.

our idealized

script submitted to JGR Oceans

a zonally uniform

zonel

at its widest (figure 1c-d). Since we use ~~the same~~ seabed geometry (and, in particular, the same ridge height) in ~~the~~ simulations, we aim to gain insight into the effect of variation in the ridge-draft gap by considering several different values of W – the vertical distance between the crest of the seabed ridge and the ice shelf base (figure 2a). W enters ~~only~~ the model ~~only~~ via the ice profile. Following De Rydt et al. (2014), we use an ice shelf draft that is given by

$$h(y) = \begin{cases} \left(\frac{310+W}{2.64}\right) \tan^{-1}\left(\frac{y}{5882}\right) - 3 & \text{for } y < y_f, \\ 0 & \text{for } y \geq y_f. \end{cases} \quad (4)$$

182 Here y_f is the variable location of the ice front (see below). We stress that these ice profiles
183 are not obtained from ice dynamics considerations, but selected for their qualitative
184 similarity to PIIS: they include a flatter section offshore of the ridge and a steeper
185 section inshore of the ridge that is observed in practice. Resembles ~~estimated by~~ basel slope from
radar &
satellite data.

186 We consider three different values of W here: $W=100$ m, $W=150$ m, and $W=200$ m.
187 The smallest value, $W=100$ m, corresponds to the minimum observed ridge-draft gap
188 in ~~the~~ Island (figure 1b,c), while the largest value, $W=200$ m, corresponds to an upper bound, above which there is little melt response to calving, as we shall see.

189 Within each experiment, the front position y_f is systematically reduced, to simulate
190 calving. The ten simulations within each experiment use values $y_f=84, 80, 75, 70,$
191 $65, 60, 55, 50, 45,$ and 40 km, which correspond to calved lengths of $l_c=0, 4, 9, 14, 19,$
192 $24, 29, 34, 39,$ and 44 km, respectively. Within each experiment, the simulation with y_f
193 = 84 km is referred to as the ‘uncalved’ simulation, serving as a benchmark against which
194 results are compared. There are both pragmatic and physical reasons for choosing this
195 particular range of values for y_f : the uncalved simulation corresponds roughly to the ob-
196 served distance of the ice front from the PIG grounding line in 2009, before significant
197 calving took place in the late 2010s; the lowest value, $y_f = 40$ km, is chosen as a com-
198 promise between allowing us to consider scenarios in which the ice front has been retreated
199 significantly beyond the ridge, whilst retaining ~~survive~~ large area that is shared by each ex-
200 periment. As we discuss further in §3, the area over which melt rates are averaged must
201 be invariant to calving for a robust assessment of the melt response to calving. The com-
202 putational expense of high resolution ocean simulations forces us to restrict the num-
203 ber of simulations within each experiment to ten. → This is
confusing:
a reduction in
 y_f means an
advance of the
ice front.
(Or is the x-axis
in fig 2 wrong?)

→ Would more simulations you do more
simulations if they were cheaper?

2.3 Hydrographic Forcing

206 For each unique value of W , we perform the experiment three times, each with a
207 different hydrographic forcing. Comparing the results of these experiments gives us an
208 indication of the sensitivity of our results to hydrographic forcing. The range of these
209 hydrographic forcings covers that which is observed in practice (see below).

210 The hydrographic forcing is imposed on the model by means of a restoring bound-
211 ary condition at the northern end of the domain: at this boundary, the temperature and
212 salinity are restored to specified vertical profiles, shown in figure 2b–c, over a distance
213 of five horizontal grid cells (total length 2 km) with a restoring timescale that varies from
214 12 hours at the boundary to 60 hours in the interior. The model includes solid walls
215 with a free slip condition at the southern, western, and eastern sides of the domain. These
216 specified temperature and salinity profiles are piecewise linear functions of depth: they
217 are constant in both an upper (temperature -1°C , salinity 34 psu) and lower layer (tem-
218 perature 1.2°C , salinity 34.7 psu), which are separated by a pycnocline of thickness 400 m
219 across which the temperature and salinity vary linearly. The pycnocline begins at a vari-
220 able depth P (a higher P corresponds to a deeper pycnocline), which parametrizes the
221 whole profile (figure 2b–c); the three hydrographic forcings we consider have $P=600$ m,
222 700 m, and 800 m.

In my mind, each simulation with a different geometry/forcing is an 'experiment'. I would class all experiments as a triplet (W, P, y_f) , which uniquely defines the geometry & forcing. The default has to be $(100, 600, 0)$ (Sect. 3), then

These piecewise linear profiles are approximations to typical conditions for Pine Island Bay (Jacobs et al., 1996; Dutrieux et al., 2014; Jenkins et al., 2018) (see figure 2a–b), where the upper and lower layers are primarily Winter Water and (modified) Circumpolar Deep Water, respectively. As mentioned, the record of hydrographic conditions in Pine Island Bay (PIB) has revealed significant variability in the depth of the pycnocline on interannual timescales (Dutrieux et al., 2014); the profiles with $P=600$ m and $P=800$ m are approximations to profiles observed in PIB in the years 2009 and 2012, respectively. These two years approximately span the range of observed conditions: in 2009, the average depth of the pycnocline was at its shallowest level on record (Webber et al., 2017), while in 2012, the average depth of the pycnocline was at its second-deepest level on record (the lowest pycnocline depth, recorded in 2013, was only marginally lower than in 2012).

The nine experiments are uniquely identified by a (W, P) pair, where $W \in \{100, 150, 200\}$ m and $P \in \{600, 700, 800\}$ m. We consider the extreme scenario with the strongest topographic barrier and the hydrographic forcing with the thickest CDW layer, $(W, P) = (100, 600)$ m to be the baseline experiment, against which the other experiments are compared; in the following section, we describe the results of the baseline experiment, before describing how this picture changes for different values of W and P in sections 4 and 5, respectively.

$(100, 600, y_f)$ in Sect. 4,

$(150-200, 600, y_f)$ in Sect. 5,

$(100, 700-800, y_f)$ in Sect. 6

3 Results for the Baseline Experiment ($W=100$ m, $P=600$ m)

In this section, we describe the results for the baseline experiment ($W = 100$ m and $P = 600$ m, solid lines in figures 2a–c). We begin by describing the steady state ocean configuration in the uncalved simulation, and then describe how, and why, the melt rate responds to calving.

↳ this is a perturbation, not a 'baseline'

3.1 Uncalved Simulation

Ice-ocean properties that characterize the default simulation are shown in figure 3. Melt rates (figure 3a) are below 20 m year $^{-1}$ everywhere, except for a region located within 20 km of the grounding line, where melt rates reach a maximum of approximately 120 m year $^{-1}$. The average melt rate over the whole shelf is approximately 20 m year $^{-1}$, this is lower than the value of 33 ± 2 m year $^{-1}$ that was estimated by Jenkins et al. (2010) based on observations in Pine Island Bay in 2009, to which the $P = 600$ case corresponds (figure 2b, c). This discrepancy is in the expected direction: this simulation corresponds to the extreme scenario in which the ridge-draft gap is set to the minimum gap that is observed in practice.

but the draft is also deeper than observed, so more are exposed to CDW?

At this point, we introduce the definition on the 'inner cavity' as the area of the ocean domain that is located within 30 km of the Southern end of the domain (red shaded region in figure 2a). We use the mean melt rate in the inner cavity, referred to as the 'inner cavity melt rate', as a single metric to quantify changes in melt rate with calving. Since the melt rate is highly spatially variable (figure 3a) it is necessary to consider a fixed area, which is common to each simulation, when assessing changes in melt rate with calving. This best demonstrated by example: integrating over the whole shelf, for example, would make smaller shelves appear to have anomalously large melt rates, since the region of high melt close to the grounding line would occupy a greater proportion of the total shelf. Our choice of 30 km in the definition of the inner cavity region reflects a compromise between including simulations in which the ice front has calved a significant distance beyond the ridge (the smallest shelf we consider must be larger than the inner cavity region if the entirety of this region is to be included in each simulation), while including a reasonably large section of the uncalved ice shelf over which the melt rate is averaged. Crucially, this choice of inner cavity includes the grounding line, a region in which changes in melt rate are acutely important for the dynamics of the ice sheet

enabling

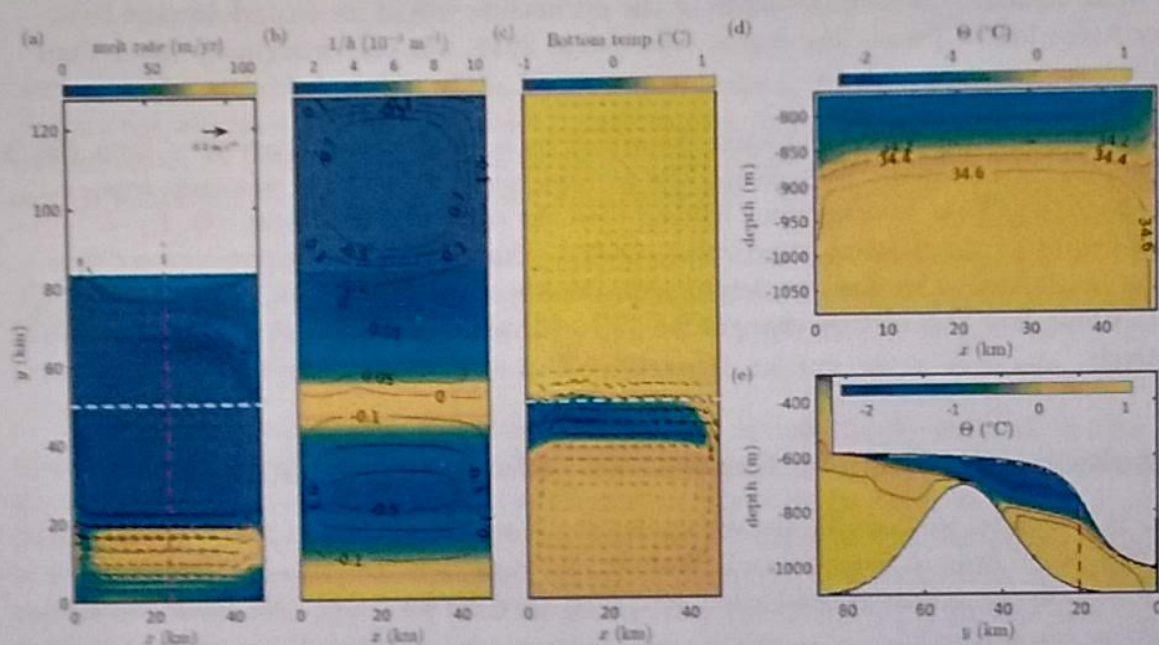


Figure 3. Ice-ocean properties that characterize the default (uncalved) simulation in the baseline experiment ($W = 100 \text{ m}$, $P = 600 \text{ m}$). (a) Melt rate (colours) and boundary layer velocities (arrows, every fifth velocity vector is plotted), averaged over the three grid cells adjacent to the ice-ocean interface. White areas correspond to open ocean. The black line indicates an arrow length that would correspond to 0.6 m s^{-1} . The white dashed line indicates the location of the top of the ridge (along which the section in (d) is taken) and the magenta dashed line indicates the meridional centre line (along which the section in (e) is taken). (b) Inverse water column thickness $1/h$ (colours) and barotropic stream function (contours, in units of Sv) at levels 0.05 (green) 0 (blue), -0.1, -0.3, -0.5, and -0.7 Sv (all black). (c) Bottom temperature (colours) and bottom current (arrows) averaged over the three grid cells closest to the seabed. The scale bar for velocity vectors in (a) is also appropriate for (c). (d) Zonal cross-section taken along the ridge crest (white dashed line in (a)) up to the ice shelf base, showing potential temperature (colours) and salinity contours at the 34.2, 34.4, and 34.6 psu levels. (e) Meridional cross-section, taken along the magenta dashed line in (a), with colours and contours as in (d). Change the zero contour to red and add the cyan anti-cyclonic circulation.

plot velocities
that define U^*
instead?

Potentially add a $\infty \begin{smallmatrix} N \\ \searrow \\ W \end{smallmatrix}$ arrow so readers can
easily identify northern boundary etc...

(Seroussi et al., 2014; Arthern & Williams, 2017). Although the values of inner cavity melt rate are dependent on the defined length of the inner cavity, we verified that the trends and key results are independent of this choice of inner cavity. The inner cavity melt rate in the uncalved run ($l_c=0$ km) is 46 m year^{-1} (figure 4a).

Melt rates depend on both the cavity circulation and thermal driving (see equation (1)). Cavity circulation (figure 3a, c) is characterized by a Coriolis-driven cyclonic circulation. This circulation is directed northward at the eastern boundary ($x=0$ km) and southward at the western boundary ($x=48$ km). In the inner cavity, the circulation is vigorous to the south of $y=30$ km, but high melt rates are restricted to south of $y=20$ km: to the north of $y=20$ km, a cold and fresh meltwater plume sits adjacent to the ice-ocean interface (figure 3e) and the thermal driving is therefore much smaller than to the south of $y=20$ km, where the ice is adjacent to warm water.

When the ice shelf is calved in the subsequent simulations, we change both the buoyancy flux (the total volume of meltwater changes), and the water column thickness in regions of the domain where the ice shelf is removed. Changes in the water column thickness can only influence the flow through barotropic dynamics; it is therefore instructive to consider the barotropic stream function for the uncalved simulation first, and assess how it changes with calving. Assuming that turbulent stresses and viscous stresses are negligible, barotropic flow conserves its potential vorticity (PV), calculated as $(f+\zeta)/h$, where h is the water column thickness and $\zeta = \partial v / \partial x - \partial u / \partial y$ the relative vorticity, with u and v the depth-averaged velocity components in the x and y directions, respectively. Conservation of PV means that flow must align with f/h contours, or gain relative vorticity. In our idealized domain, contours of constant water column thickness correspond to lines of constant y , aligned east-west (figure 3b). The ice front and the seabed ridge are the two main discontinuities in the water column thickness, and therefore act as PV barriers; these PV barriers divide the domain up into three regions of closed f/h contours: inshore of the ridge, offshore of the ridge (but under the ice shelf), and the open ocean.

Regions of closed f/h space promote gyre formation because the flow must gain relative vorticity at their boundaries. Offshore of the ridge, a weak anti-cyclonic circulation spins up. Meltwater that crosses the ridge into this region from the inner cavity experiences an increase in water column thickness (reduction in $1/h$); in order to maintain a constant PV, the ocean must gain relative vorticity diverting the flow anti-clockwise (increasing $\partial v / \partial x$ and/or reducing $\partial u / \partial y$). Similarly, as flow approaches ridge along the seabed, it is diverted eastward (figure 3a). Ultimately, however, the PV barrier in this 'narrow gap' case is sufficiently strong that little flow is able to penetrate across the ridge (note the zero barotropic contour at the top of the ridge in figure 3b). The exception to this is a strong boundary current at the eastern boundary, where flow divergence permits a southward flow perpendicular to contours of constant column thickness. The ridge crest PV barrier means that barotropic flow is unable to leave the cavity resulting in a strongly topographically controlled cyclonic circulation inshore of the ridge.

Away from the barotropic dynamics, the presence of meltwater sets up a zero depth-mean, vertically sheared overturning circulation. Although this flushes the inner cavity, it does so far more weakly than even a moderate barotropic flow is able to. As discussed, the potential vorticity barrier provided by seabed ridge and ice shelf draft prevents barotropic flow across the ridge; in the absence of significant flow across the ridge, the inshore side of the ridge hosts meltwater. Water entering at the Eastern boundary mixes with this meltwater as it crosses the ridge; warm water that enters the inner cavity is lightly modified by this mixing, resulting in a bottom temperature that is slightly cooler (approximately 0.8°C) inshore of the ridge than offshore (approximately 1.3°C , see figure 3c, e). This intrusion of warm water affects melting by both providing significant heat to the inner cavity, and increases the stratification and thus speed of the topographically confined cyclonic circulation.

~~As for as I
can see, no
recirculation is present
to fig 3~~

} OR show thermal
driving ..

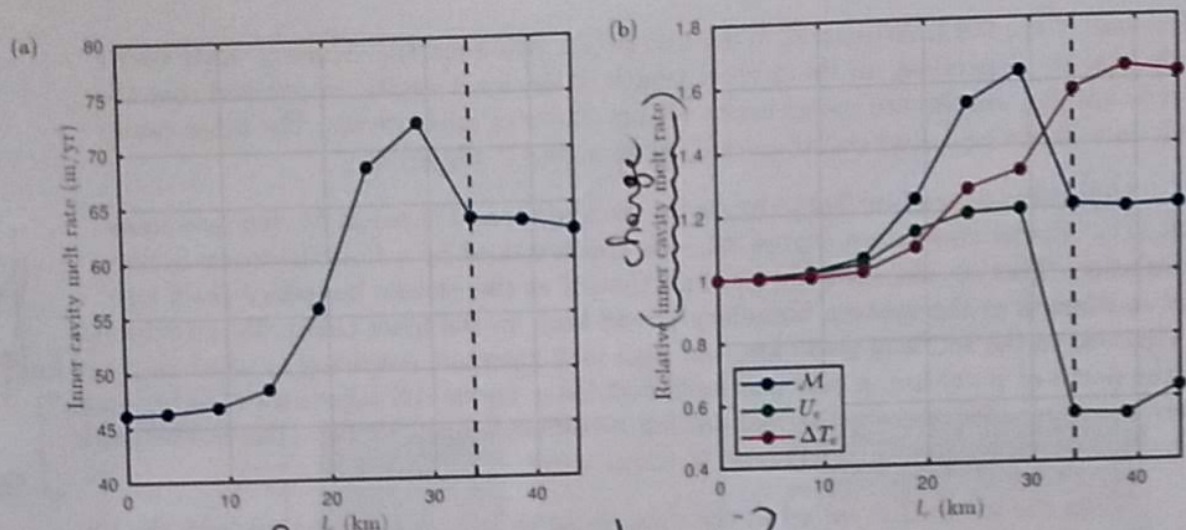
change its

} but this is a
baroclinic flow

} Can you calculate
the volume transport
in m^3/s across
the ridge and
into the deep
cavity? I
suspect this is
not 'negligible'.

fig 3c ?
←

do you mean
meltwater
is recirculated
rather than
flushed out?



Show y_1 as separate x-axis?

Figure 4. (a) Mean inner cavity melt rate as a function of the calved length l_c . The black dashed line indicates the position of the ice front when it is located directly above the seabed ridge. (b) Velocity-thermal driving decomposition: decomposition of changes in inner cavity melt rate relative to the uncalved simulation into changes in boundary layer speed U_e (green curve, equation (5)) and thermal driving ΔT_e (red curve, equation (6)). The blue curve indicates the change in melting relative to the uncalved simulation (equation (7)).

326 In summary, in this uncalved simulation, which has a strong barrier restricting CDW
 327 access to the inner cavity, a topographically constrained cyclonic circulation is spun up
 328 inshore of the ridge. A strong current at the eastern boundary provides the inner cav-
 329 ity with lightly modified warm water. The presence of this warm water enhances melt-
 330 ing by both providing more heat and resulting in a stronger circulation in the inner cav-
 331 ity.

§ 4

3.2 Calving Response

332 The inner cavity melt rate as a function of the calved length l_c is shown in figure 4.
 333 We see that, while the ice shelf front is located far offshore of the ridge ($l_c < 14$ km),
 334 removing sections of ice results in only a weak increase in the inner cavity melt rate.
 335 However, as the ice shelf front is retreated further towards the ridge, the melt rate increases
 336 dramatically, reaching a maximum of 73 m year^{-1} (70% larger than in the uncalved run)
 337 when the ice shelf is located approximately 5 km north of the ridge crest. Perhaps sur-
 338 prisingly, retreating the ice front slightly further to sit directly above the ridge crest re-
 339 sults in a significant decrease in the inner cavity melt rate of approximately 15% (from
 340 73 m year^{-1} to 64 m year^{-1}). Finally, the inner cavity melt rate is approximately inde-
 341 pendent of ice front position when the ice front is located inshore of the ridge ($l_c > 34$ km).
 342

343 To understand the reasons for this variation in melt rate with calving, it is instruc-
 344 tive to return to equation (2), which indicates that the melt rate is approximately pro-
 345 portional to the product of the boundary layer velocity and thermal driving. We use this
 346 to investigate the relative roles of variations in both of these quantities in the changes
 347 to the inner cavity melt rate. To do so, we replace the boundary layer velocity and ther-
 348 mal driving fields in each simulation with the corresponding fields from the uncalved sim-
 349 ulation, and calculate the resulting inner cavity melt rate relative to the actual inner cav-
 350 ity melt rate from that particular simulation (Millgate et al., 2013). Explicitly, the rel-
 351 ative effect of changes in boundary layer velocity and thermal driving on the inner cav-

352 } Where do you
 353 do this?

To me this suggests calculating $\frac{\int u^*(l_c) \Delta T(l_c=0)}{\int u^*(l_c=0) \Delta T(l_c=0)}$
 $\neq \int \frac{u^*(l_c)}{u^*(l_c=0)}$

ity melt rate are assessed by computing

$$U_e(l_c) = \int_{\text{inner cavity}} \frac{u^*(x, y; l_c)}{u^*(x, y; l_c = 0)} dx dy, \quad (5)$$

$$\Delta T_e(l_c) = \int_{\text{inner cavity}} \frac{T(x, y; l_c) - T_b(x, y; l_c)}{T(x, y; l_c = 0) - T_b(x, y; l_c = 0)} dx dy, \quad (6)$$

where $u^*(x, y; l_c = 0)$, $T(x, y, l_c = 0)$, and $T_b(x, y, l_c = 0)$ are the boundary layer velocity, ocean temperature, and local freezing temperature that emerge from the uncalved simulation. The quantities in (5)–(6) are compared, for a given calved length l_c , to the relative change in melting over the default simulation,

$$\mathcal{M}(l_c) = \int_{\text{inner cavity}} \frac{\dot{m}(x, y, l_c)}{\dot{m}(x, y, l_c = 0)} dx dy. \quad (7)$$

The quantities (5)–(7) are plotted in figure 4b as a function of l_c . Here, a melt response to calving that results exclusively from changes in the thermal driving would be indicated by indistinguishable blue and red curves, and a green curve that always takes the value one, while a melt response that results exclusively from changes in boundary layer velocity would be indicated by indistinguishable blue and green curves, and a red curve that always takes the value one. We refer to this comparison as a ‘velocity-thermal driving decomposition’ henceforth.

The velocity-thermal driving decomposition (figure 4b) indicates that both changes in the boundary layer velocity and thermal driving play an important role in the melt response to calving in this experiment (i.e. neither plays a dominant role). When the ice front is located offshore of the ridge ($l_c < 25$ km), ice front retreat results in increases in both the boundary layer velocity and thermal driving; these increases are complementary, they act in unison to increase the inner cavity melt rate with calving. When the calving front is retreated to sit above the ridge, the thermal driving effect increases further, while the velocity effect decreases sharply, indicating a significant reduction in the inner cavity circulation; further, this reduction in cavity circulation outweighs the increase in thermal driving, leading to an overall reduction in the inner cavity melt rate when front is retreated to sit directly above the ridge. When the ice shelf is calved further, both the thermal driving and boundary layer velocity are approximately constant.

As mentioned, calving changes both the buoyancy forcing and the water column thickness, with the latter having an impact only via barotropic dynamics. To understand the reasons for the changes in thermal driving and boundary layer velocity, it is there instructive to consider how the barotropic stream function changes as the ice front is retreated (figure 5a). We focus first on those cases in which the ice front is located some way (more than 10 km) offshore of the ridge (i.e. $l_c < 14$ km); these cases are qualitatively similar to the uncalved case: the strong PV barrier provided by the ridge and ice draft remains in place and a topographically constrained cyclonic circulation is spun up inshore of the ridge, with a weak anti-cyclonic circulation offshore of the ridge. There is zero barotropic flow between these two regions (i.e. across the ridge) except for at eastern boundary (figure 5a). Warm water flows across the ridge at the eastern boundary, and is modified by mixing with the meltwater plume as it does so. As the ice front retreats, the meltwater plume becomes marginally less prominent (figure 5b–c) and mixing at the eastern boundary is reduced slightly. As a result, the temperature of the warm water that enters the cavity increases slightly; this has the double effect of both increasing the heat available for melting and increasing the stratification – and thus strength of the circulation – of the inner cavity.

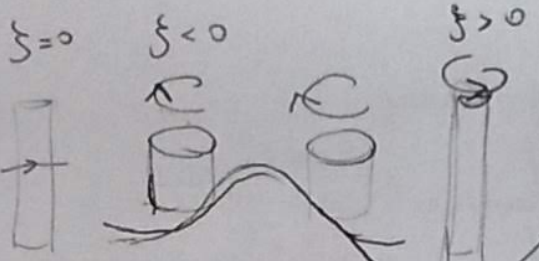
As the ice front is retreated and nears (but does not pass) the ridge, the two PV barriers (the ice front and the seabed ridge) approach one another, and the anticyclonic circulation in the outer cavity is no longer seen. Despite the ridge crest and ice draft still providing strong PV barriers, a significant barotropic flow is able to cross the ridge. This

? Can no longer be sustained.
13-

plots suggest
? $\psi = 0$ @
eastern boundary
too

Dreaming... doodling... ignore!

Manuscript submitted to JGR Oceans



Not saying
you should remove
these, but they are
not explicitly discussed.

Are they strictly
needed or can
we save ink?

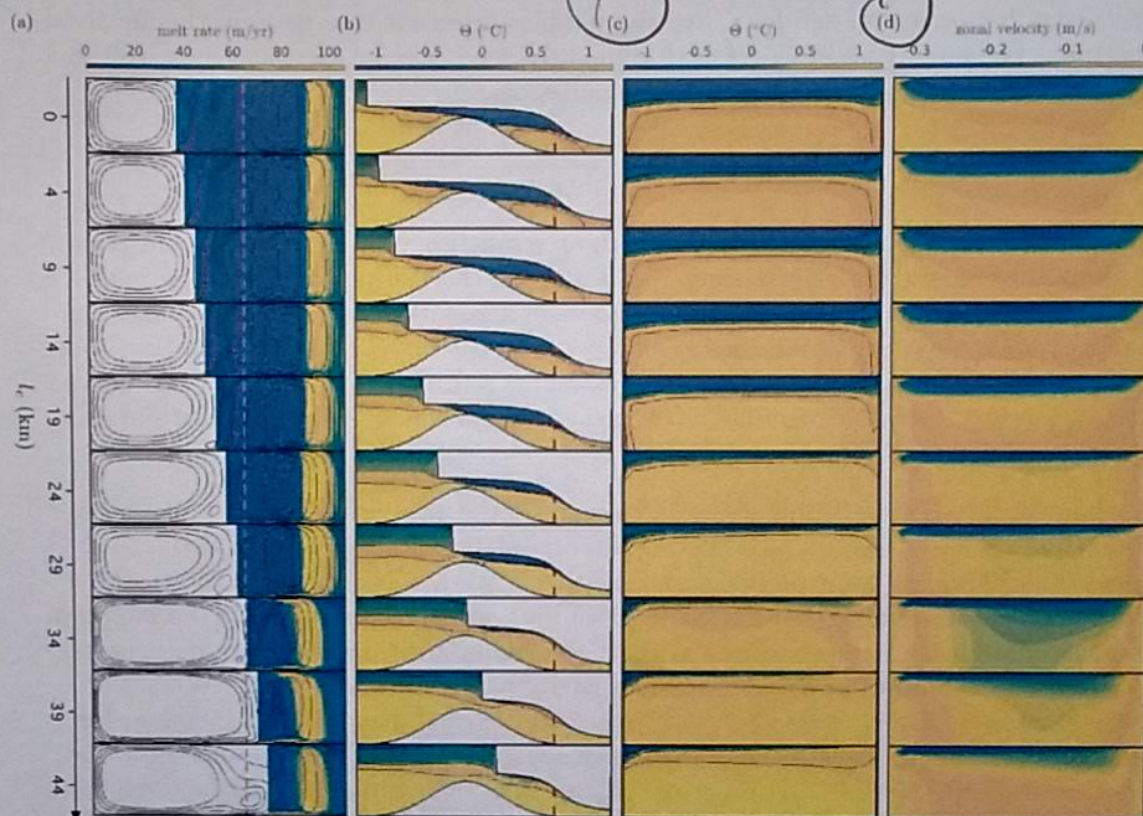


Figure 5. (a) Contour plots of melt rate (colours) and barotropic stream function (contours, black at -0.1, -0.3, -0.5, and -0.7 Sv levels, magenta at the 0 Sv level, and green at the 0.05 Sv level) in the idealized simulations with $P = 600$ m and $W = 100$ m. The calved length l_c increases from 0 km in the first row to 44 km in the final row. The white sections indicate open ocean. (b) Contour plots of potential temperature Θ (colours) and salinity (contours, at levels 34.2, 34.4, and 34.6 psu, as in figure 3, black arrows indicate the direction of increasing salinity) taken along the centreline of the domain (magenta dashed line in figure 3a). The white section at the top and bottom of each subplot indicate the ice shelf and seabed ridge, respectively. (c) Contour plots of potential temperature (colours) and salinity (contours, at levels 34.2, 34.4, and 34.6 psu) along a zonal section located 20 km downstream of the grounding line. (d) As in (c) with colours indicating the zonal velocity. In each case, the colour bar at the top of the column is appropriate for each row in the column. (Note that the first row in columns (a), (b), and (c) in the first row show the same data as in figure 3(a), (d), and (e), respectively.)

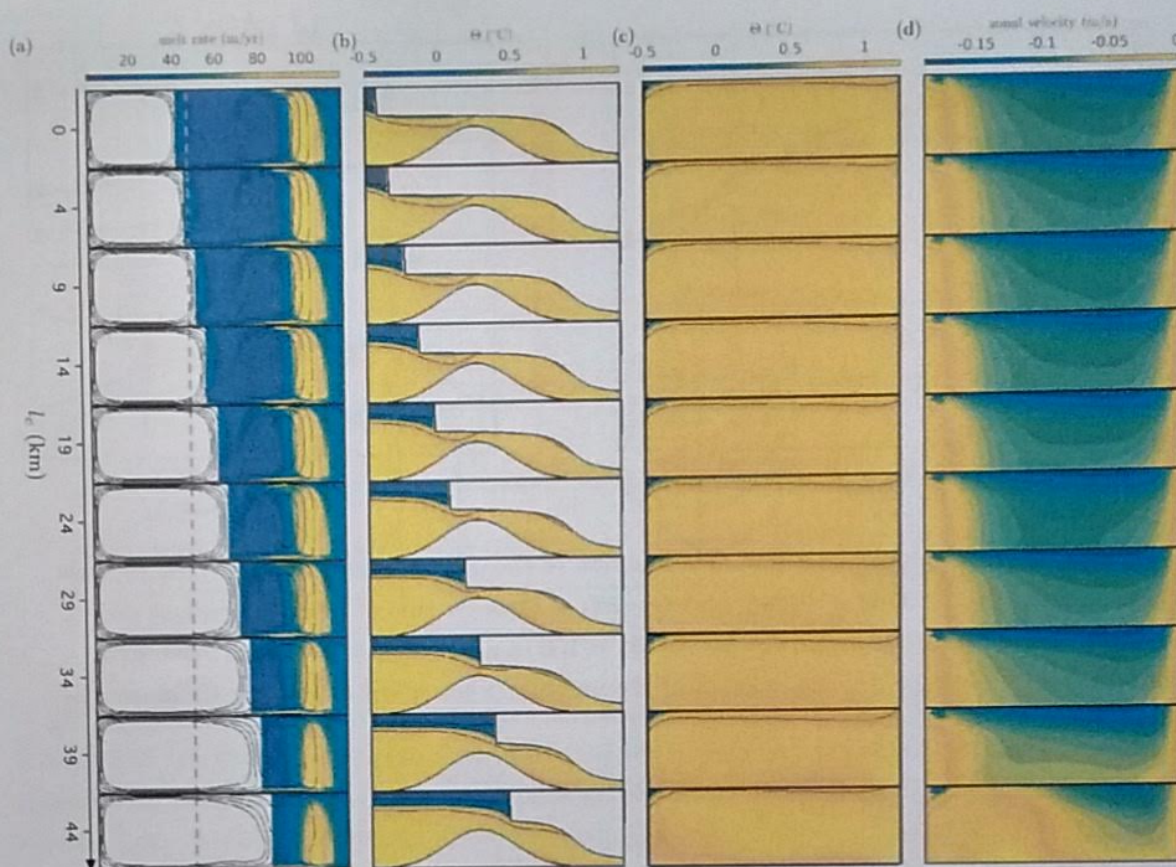


Figure 7. Ocean characteristics in the idealized simulation with $P=600$ m and $W=200$ m.
This plot is as in figure 5 for the simulation with $W=200$ m.

duction in inner cavity melt rates for values of l_c above that at which the maximum melt rate is attained results from a reduction in the inner cavity circulation, which outweighs an increase in thermal driving. There are, however, two important differences to the $W=100$ m case: firstly, the inner cavity melt rate is far less sensitive to calving for both $W=150$ m and $W=200$ m cases (the difference between largest and smallest inner cavity melt rates is approximately 20% and 10%, respectively, compared to 70% for $W=100$ m). Secondly, these larger gap scenarios do not display a threshold-like behaviour, where the inner cavity melt rate drops suddenly as the calving front reaches the top of the ridge, as it does in the $W=100$ m case. These observations are consistent with the results of De Rydt et al. (2014), who identified that the melt rates in a similar idealized domain are largely independent of the ridge-draft gap when it is larger than approximately 200 m.

To understand these results, it is useful to compare the barotropic streamfunction, and zonal and meridional cross sections that were shown in figure 4 for $W=100$ m to those in figure 7 for the $W=200$ m case. (A comparison between the $W=100$ m and $W=150$ m cases is qualitatively similar to that discussed below, but the differences are clearer for $W=200$ m.) Recall that in the $W=100$ m case, two PV constraint considerations are fundamental to the response: (1) when the ice front is offshore of the ridge, the ridge-draft PV barrier prevents barotropic flow into the cavity and inner cavity flushing is weak, but (2) ice front induced vorticity and the relaxation of this PV barrier as the ice front is retreated to the ridge and beyond permits a barotropic flow to efficiently flush the inner cavity with warm water. In the $W=200$ m case, the ridge-draft PV barrier is somewhat weaker than in the $W=100$ m case, and barotropic flow across the ridge occurs, even when the ice front is located offshore of the ridge (figure 7). The regime in which barotropic flow across the ridge is entirely blocked is never realized; the system behaves as in the ‘highly calved’ regime for all values of l_c . As a result, the inner cavity is almost

→ pfeew

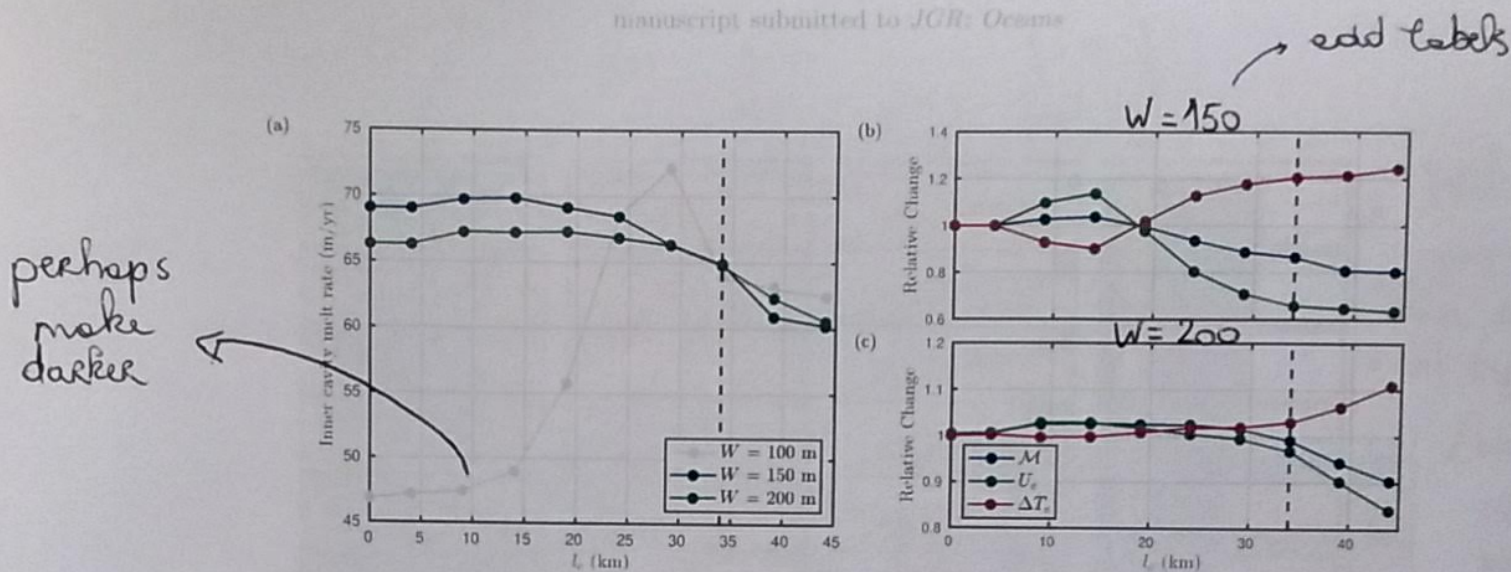


Figure 6. (a) Inner cavity melt rate as a function of the calved length l_c for $W=100$ m (light grey, as in figure 4a), $W=150$ m (blue), and $W=200$ m (green). (b)-(c) Velocity-thermal driving decomposition (i.e. as in figure 4b) for (b) $W = 150$ m and (c) $W = 200$ m. In each plot, the black dashed line indicates the position of the ice front when it is located directly above the seabed ridge.

is because the ice front induces vorticity in the water column through lateral shear, and this vorticity source allows the barotropic flow to break the f/h constraint (note the ice front provides a source of vorticity wherever it is located, but its effect is most noticeable when the vorticity is provided adjacent to the strong PV barrier that the ridge provides). The resulting barotropic flow across the ridge is far more vigorous at flushing the inner cavity than the overturning circulation that flushes the cavity when the ice front is located further offshore; as a result, the inner cavity is entirely flooded with warm water (figure 5c). Although this means there is far more heat available for melting (thermal driving effect increases when calving on top of the ridge, figure 4b), this is outweighed by the reduced stratification and thus reduction in the velocity in the inner cavity (figure 5d).

ice front coincides with the ridge crest

Once the ice front is retreated beyond the ridge, the strong PV barrier provided by the ridge crest and ice draft is relaxed. The seabed ridge alone provides a much weaker f/h constraint than the ridge and draft, so barotropic flow is able to cross the ridge. The cavity is again efficiently flushed with warm water, resulting in strong thermal driving but weak stratification. Melt rates become independent of ice front position once the ice front has retreated beyond the ridge, indicating that the ridge is only influential because it has an ice shelf overlying it. *and, as will be shown later, the ice-bed gap is small enough.*

§5

Effect of Cavity Geometry on Melt Response to Calving

In the previous section, we analyzed how the inner cavity melt rate responds to ice front retreat, and identified the mechanisms responsible, in the $W=100$ m case. The strength of the topographic barrier that restricts warm water access to the inner cavity was identified as an important control on this response. In this section, we describe how this picture changes for larger values of W (explicitly, $W=150$ m and $W=200$ m), which are expected to have a weaker topographic barrier *in particular*.

Mean melt rates as a function of calved length l_c for $W=150$ m and $W=200$ m are plotted in figure 6a. As in the $W=100$ m case, the inner cavity melt rate reaches a maximum when the ice front is located offshore of the ridge crest. In addition, the velocity-thermal driving decomposition indicates that for both $W=150$ m and $W=200$ m, the re-

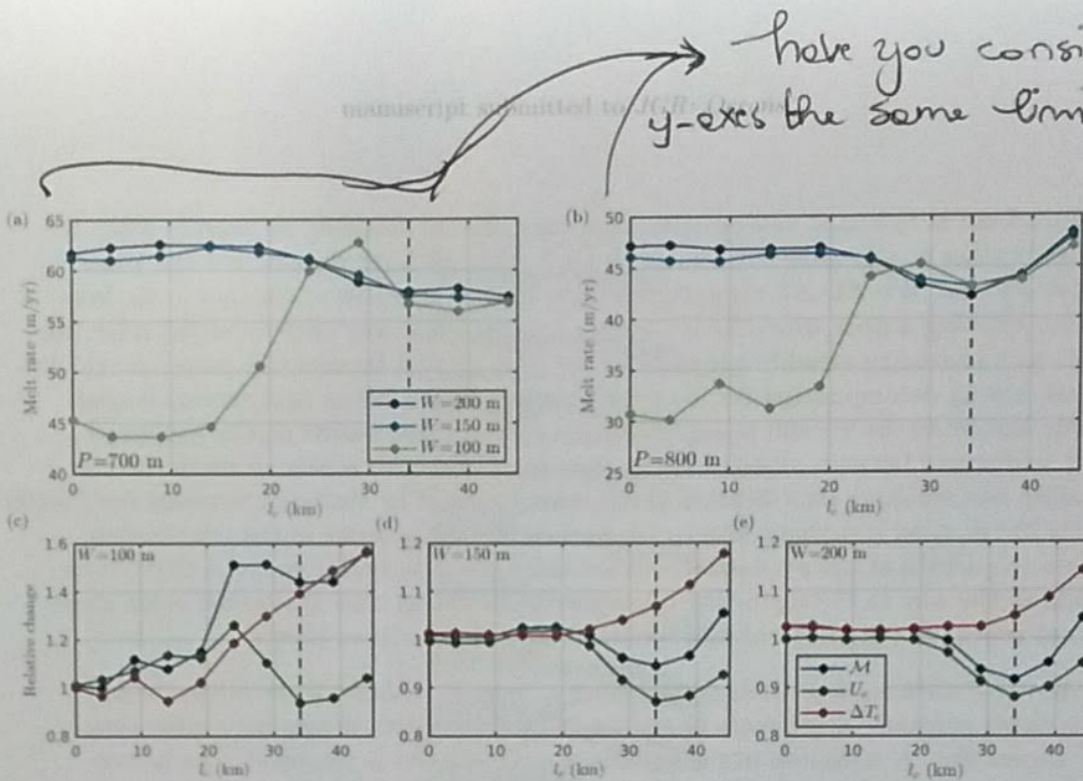


Figure 8. (a)–(b) Inner cavity melt rate as a function of calved length l_c in idealized simulations with (a) $P=700$ m and (b) $P=800$ m. Colours correspond to different values of W , as indicated by the legend in (a). The black dashed line indicates the location of the crest of the sea-bed ridge. (c)–(e) Velocity–thermal driving decompositions (as in figure 4) for the data shown in (b): (c), (d), and (e) correspond to the results for $W=100$ m, $W=150$ m, and $W=200$ m, respectively, as indicated.

437 entirely flushed with modified CDW (figure 7b), regardless of the ice front position. Ice
438 front retreat, which permits increased warm water access, has only a limited effect, in
439 particular, this removes the tendency for both increasing temperature and circulation
440 that we see in the $W=100$ m case, before the ice front is retreated to the ridge.

441 Although there is barotropic flow across the ridge for all values of l_c , when the ice
442 front is retreated to – and beyond – the ridge, the ice front induced vorticity and the re-
443 laxation of the PV barrier mean that barotropic flow across the ridge increases further.
444 As a result, the inner cavity stratification reduces (figures 6c and 7b) ~~and~~ as does the
445 melt rate (figure 6a). However, the change in f/h when the front is retreated beyond the
446 ridge is not as severe, and thus the increase in barotropic flow is not as acute, as in the
447 $W=100$ m case, and the sharp reduction in melt rates is not observed.

86

Effect of Hydrographic Conditions on Melt Response to Calving

449 Before moving on to assess how the inner cavity melt rate responds to calving in
450 the realistic simulations, we briefly consider how the picture presented in the previous
451 two sections changes depending on the hydrographic forcing. Since we consider a con-
452 stant ridge height, variations in the difference between the pycnocline depth and the depth
453 of the ridge crest – which we expect to be a key driver of the quantity of warm water
454 that is able to spill over the ridge and into the inner cavity – is captured here by vari-
455 ability in the value of P . (Fig. 2)

456 The inner cavity melt rate and velocity–thermal driving decomposition for the three
457 experiments with $P=700$ m (hydrographic forcing as in the dashed profiles in figures 2b
458 and c) and the three experiments with $P=800$ m (dot-dashed profiles) are plotted in fig-
459 ure 8. The results for $P=700$ m are similar to those for $P=600$ m: for the narrowest gap
460 ($W=100$ m), the inner cavity melt rate is sensitive to the front position, increasing rapidly

as the ice front is retreated towards the ridge crest, before dropping off sharply when the ice front reaches it, and does not change under further ice front retreat. For the wider gaps ($W=150$ m, $W=200$ m), the melt rates are far less sensitive to changes in ice front position, reaching a peak when the ice front is located some way offshore of the ridge (figure 8a) and decreasing steadily with further ice front retreat beyond this point. A velocity-thermal driving decomposition for the experiments with $P=700$ m (not shown) is qualitatively similar to the $P=600$ m case discussed above: these results can be explained by the interaction between changes in the amount of heat that is able to reach the inner cavity and resulting stratification of the inner cavity. The similarity between the $P=600$ m and $P=700$ m cases is perhaps unsurprising when framed in terms of the relationship between the depths of the pycnocline and the ridge crest: in both cases, the CDW layer extends all the way to the top of the ridge (see figure 2) and thus the seabed ridge alone does not provide a significant barrier to CDW access to the inner cavity.

In the $P=800$ m case, while the ice front is located offshore of the ridge, the melt rate is either constant or increases as the ice front is retreated, depending on the value of W (figure 8b). A reduction in the boundary layer velocity is responsible for a drop in inner cavity melt rates as the ice front is retreated towards the ridge crest (figure 8c-e), as in the $P=700$ m and $P=600$ m cases. Beyond this point the $P=800$ m case differs: calving taking the ice front beyond the ridge results in an *increase* in the inner cavity melt rate (figure 8b), which is associated with a reversal of the reduction in boundary layer velocity (figure 8c-e) (i.e. the boundary layer velocity increases on average when the ice front is retreated beyond the ridge). The important difference in this case that the seabed ridge alone is able to provide a significant barrier, preventing warm water from reaching the inner cavity, since the CDW layer in the outer cavity does not extend to the top of the ridge (figure 9). Therefore, the inner cavity is not flooded with CDW after the ice front is retreated to sit above the ridge crest and subsequent ice front retreat increases the stratification further. This leads to a strengthening of the circulation, working in tandem with increased heat content to increase the inner cavity melt rate.

Ignore this. Boundary layer discussions only, not most sensitive to P for \S 2-5

§7

Assessing the Melting Response of PIIS to Calving

The experiments described in §2–5 reveal how melt rates near the grounding line in idealized geometries with a uniform ridge-draft gap may respond sensitively to calving. This response is heavily dependent on the geometry of the cavity and, in particular, the gap between the ice draft and seabed ridge. These idealized experiments inform our understanding of a similar experiment that is designed to assess the response of melt rates to PIIS calving. In this section, we describe this experiment, and present and analyze the results.

6.1 Experiment Details

To assess the response of sub-shelf melt rates on Pine Island Ice Shelf to calving, we resolve the circulation in a PIG cavity geometry (described below), using the ocean model described in §2.1. We consider six different ice shelf topographies, each of which has a unique ice front position. The locations of these ice fronts are shown in figure 10: the first simulation (darkest purple curve in figure 10a) uses an ice shelf ~~cavity~~ that corresponds to PIIS in 2009. The second simulation (second-darkest purple ice front in figure 10a) uses the 2009 ice shelf draft, but with a section of ice removed so that the ice front matches that in 2020. The four further simulations similarly use the 2009 ice shelf draft but with sections of fast flowing ice (i.e. within the shear margins) removed. We stress that the ice thickness, and thus grounding line position and ice shelf draft, at existing shelf locations remains the same in each simulation, and only the ice front position varies between simulations.

I wonder if a description of the geometry is also better placed in §2 and §6 and is used to present/discuss the results.

What is your data source? Bedmachine?
OK - I would refer to Dutrieux 2014 here already.

geometry

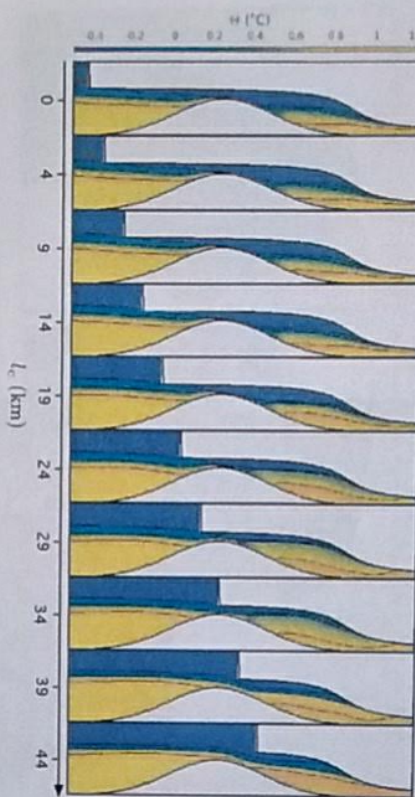


Figure 9. Meridional cross sections for simulations with $P=800$ m, $W=100$ m. This plot is as in figure 5b for the simulation with $P=800$ m, $W=100$ m.

The sub shelf cavity geometry we use is computed from the ice and seabed geometry, as described by Dutrieux et al. (2014). Briefly, the ice shelf geometry is calculated from a 40 m-resolution digital elevation model (DEM) of the ice freeboard from 2008 (Korona et al., 2009), that is adjusted with a constant median bias from observations obtained from the Autosub underwater autonomous vehicle (Jenkins et al., 2010). The DEM assumes freely floating ice throughout the shelf, which may reduce its accuracy close to the grounding line. Over the continental shelf, the seabed geometry is well known from ship echo-sounding (Dutrieux et al., 2014), while in the cavity it is calculated from an inversion of gravimetry data and corrected point-wise using the median difference between the depth from the gravimetry inversion and the Autosub observations.

We consider a single hydrographic forcing, corresponding to observed 2009 conditions in Pine Island Bay (dark grey line in figure 2b–c), to which the ocean is restored far from the ice shelf. All model parameters are as described in §2.1. In particular, we take the drag coefficient in the three equation formulation of melting to be 4.5×10^{-3} , this value is tuned so that the total meltwater flux in the simulation with the 2009 geometry (86 Gt yr^{-1}) closely matches the estimated total meltwater flux for 2009 ($80 \text{ km}^3/\text{yr}$) (Dutrieux et al., 2014)).

As mentioned in §2.1 the ridge-draft gap under PIS is not uniform but varies from approximately 100 m at its thinnest to 400 m at its ~~thickest~~ widest. The ridge-draft gap (inset in figure 10) can be approximately partitioned into a northern portion where the gap is relatively thin and a southern portion where the gap is relatively wide. A region of locally elevated f/h running east-west (solid red line in figure 10b) meets the north-south aligned seabed ridge at the junction between these wide and narrow sections (see figure 10), this east-west aligned section extends all the way to the grounding line, partitioning the region inshore of the main (north-south) ridge into a northern inner cavity (cyan box in figure 10a) and a southern inner cavity (magenta box). The east-west aligned section of higher f/h provides a PV barrier between the two inner cavity regions, which are there-

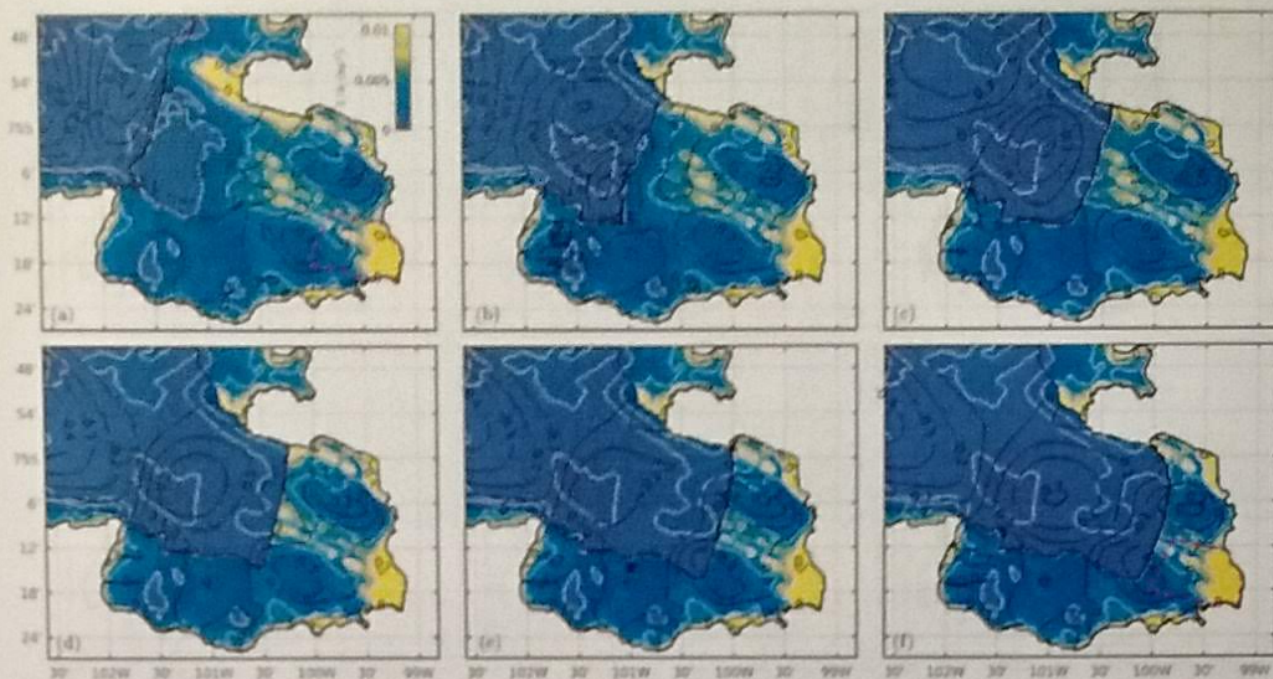


Figure 11. Simulated barotropic stream function (labelled black contours) and inverse water column thickness $1/h$ (colours and grey contours at levels corresponding to 200, 400, 600, 800, and 1000 m water column thickness). Magenta and cyan dashed boxes in (a) and (f) indicate the extent of the north and south inner cavity regions, respectively, as in figure 10.

fore approximately dynamically disconnected (figure 11a). In the following, we therefore evaluate the melt response to calving in the inner cavity regions separately.

6.2 Results

Melt rates (figure 12a) and cavity circulation (figure 11a) in the uncalved (2009) simulation are qualitatively similar to the corresponding idealized simulations. Melt rates are concentrated near to the grounding line, reaching a peak of approximately 120 m yr^{-1} several kilometers downstream of it, while remaining below 20 m year^{-1} over the majority of the shelf. This pattern of simulated melt rates under PIIS is consistent with observations (Dutrieux et al., 2013) and other numerical simulations of cavity circulation under PIIS (Heimbach & Losch, 2012). A cyclonic circulation spins up within each of the inner cavity sections, as well as in the outer cavity between the seabed ridge, and in the open ocean offshore of the ice front. Barotropic streamfunction contours largely follow the contours of constant water column thickness (figure X).

Figure 12b–f contains plots of the non-cumulative melt rate anomalies for the other five simulations in the experiment. To be explicit, non-cumulative here means that red (blue, respectively) locations on these maps indicate areas in which the melt rate increases (decreases) when the ice front is retreated from its position in the next largest ice shelf, i.e. changes in melt are shown relative to the previous simulation in the series, rather than relative to the first (2009) simulation.

When the ice front is retreated from its 2009 position to its 2020 position, melt rates within 10 km of the ice front increase significantly (figure 12b). This is attributed to high velocities associated with upwelling at the new ice shelf front, as well as the formation of a reasonably strong gyre in the newly exposed open ocean which is covered by the ice shelf in the 2009 simulation (figure 11b). This double gyre pattern is qualitatively similar to observations taken in PIB in 2020 (Yoon et al., 2021). The gyre adjacent to the shelf results in a strong circulation along the front, which itself acts as a dynamic barrier

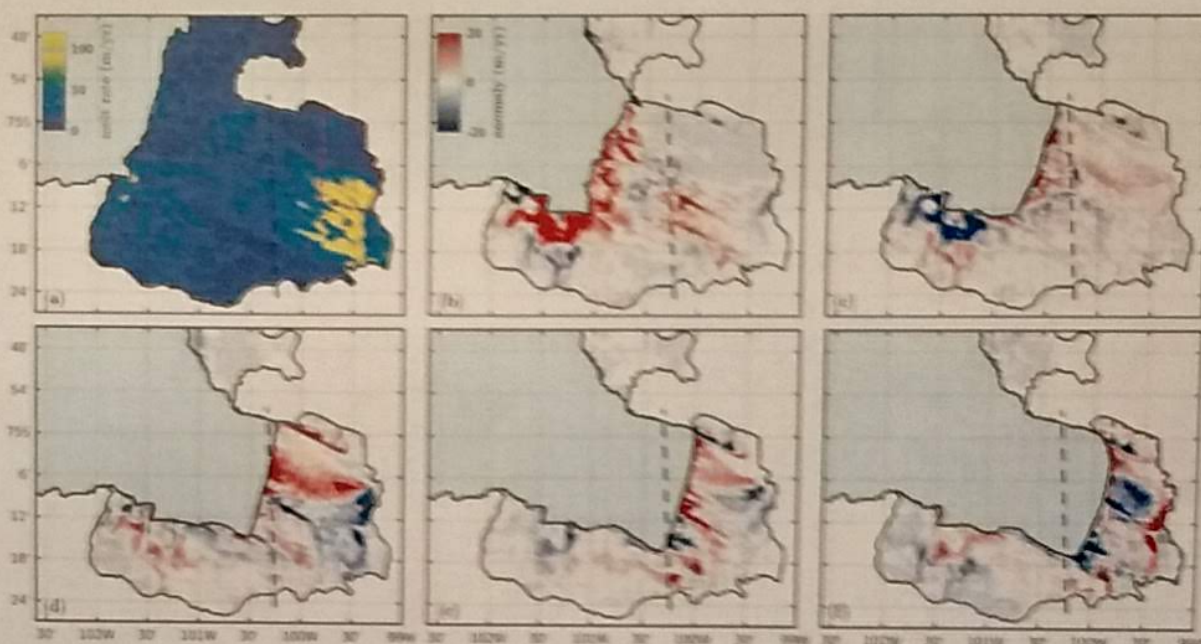


Figure 12. (a) Simulated melt rate in the 2009 Pine Island geometry. Cyan and magenta dashed boxes (also in (f)) indicate the north and south inner cavity regions (see figure 10), where the highest melt rates are concentrated. (b)–(f) Non-cumulative melt rate anomaly in the simulations (i.e. measured relative to the previous panel). The colourbar in (b) is appropriate for each of (b)–(f). In each case, the ice shelf front and 2009 grounding line from (Joughin et al., 2010) are shown as a solid black line, and the approximate location of the ridge crest as a black dashed line.

563 to flow, as well as providing a freshwater source to further enhance the flow. Melt rates
 564 in ~~the~~ both inner cavity regions do not change significantly when the ice front is retreated
 565 from its 2009 position to its 2020 position: the average melt rate in the northern and southern
 566 boxes increases by approximately 1 m year^{-1} and 2 m year^{-1} respectively (figure 12b).

567 Melt rates in the simulations with ice fronts retreated beyond the 2020 position dis-
 568 play complex patterns of change, which include large regions of both positive and neg-
 569 ative anomalies (figure 12c–f). Melt rates do not change significantly in the first ‘future’
 570 scenario, in which the ice front is still located some way offshore of the ridge, in qual-
 571 itative agreement with the idealized results. Melt rates in the vicinity of the northern
 572 shear margin increase dramatically when the ice front is retreated to a position that sits
 573 (approximately) above the seabed ridge (figure 12d), and this region of enhanced melt
 574 rates extends almost all the way to the grounding line. With the ice front immediately
 575 above the seabed ridge, the outer cavity region no longer exists; this is reminiscent of
 576 the idealized results in which there is a qualitative change in the behaviour when the outer
 577 cavity disappears and the only remaining regions of closed f/h space are the inner cav-
 578 ity and open ocean. This large melt rate anomaly is accompanied by a change in the di-
 579 rection of the circulation in the open ocean (figure 11d), which is consistent with con-
 580 servation of PV: prior to retreat beyond the ridge, melt water leaving the cavity did so
 581 offshore of the ridge, where the water column thickness increases in the direction of flow;
 582 conservation of potential vorticity requires flow to be diverted clockwise. However, when
 583 the ice front is located inshore of the ridge, the water column thickness reduces at the
 584 ice front, and conservation of potential vorticity thus requires flow to be diverted anti-
 585 clockwise, setting up an anti-cyclonic circulation in the embayment.



To go beyond these qualitative comparisons, we plot the mean melt rate as a function of calved length for both of the inner cavity regions in figure 13. In the northern region, mean melt rates remain approximately constant until the ice front approaches the seabed ridge, where they increase sharply, before remaining approximately constant as the ice front is retreated further. In the southern box, melt rates are less variable (in terms of percentage change), but the overall trend is that the melt rate increases while the ice front is located downstream of the seabed ridge, before dropping temporarily when the ice front is retreated to the ridge and subsequently increasing again.

Our interpretation of these results is guided by the idealized simulations presented in §3–5. In the northern box, the inner cavity is shielded by a relatively narrow gap between the seabed ridge and the ice draft (inset of figure 10a), and the change in melt rates with calving behaves in a qualitatively similar way to idealized results with narrower gaps ($W \leq 150$ m). A velocity-thermal driving decomposition of these changes in melt rates (figure 13b) indicates that – as in the corresponding idealized case – both increases in thermal driving and velocity contribute to the increases in melt rate with calving while the ice front is located offshore of the ridge, and that a reduction in the boundary layer velocity is responsible for the decrease in melt rates when the ice front is retreated beyond the ridge. This suggests that the enhancement in melt rates with calving while the ice front is located offshore of the ridge is driven by increased heat reaching the inner cavity and concomitant increase in stratification, while the reduction in melt rates when the ice front is retreated to the ridge results from a flooding of the inner cavity with warm water, leading to a reduction in stratification.

The southern inner cavity region sits inshore of a relatively wide gap between the seabed ridge and the ice draft (figure 10). As was the case for idealized simulations with wide gaps ($W \geq 200$ m), the mean melt rate is far less insensitive to the ice front position than it is with a narrow gap (i.e. for the northern box): the difference between the minimum and maximum melt rates in the southern box is approximately 6%, which is almost half of the corresponding value in the northern box. This invariance under calving suggests that the inner cavity is flushed with warm water in each simulation; calving, which acts primarily to increase heat content in the inner cavity, has little effect.

§8 Discussion

The results of the previous section suggest that the recent calving of PIG has not lead to increases in melting in either the shear margins or near the grounding line, which are particularly important for buttressing of the grounded ice sheet (Fürst et al., 2016; Reese et al., 2018). As a result, we do not expect that further buttressing losses associated with increased melt will take place as a result of the recent calving; this provides a negative feedback on ice shelf loss: the recent calving led to an acceleration of the grounded ice, and thus an increase of the flux of ice into the shelf; to maintain a constant ice shelf mass balance, melting must therefore increase. The lack of increase in melting after the 2020 calving therefore shifts the shelf mass balance towards positive, i.e. it promotes regrowth of the ice shelf.

However, if calving maintains its pace since 2015, the situation where the ice front sits above the ridge-crest will be realized in the mid 2020s. Large melt anomalies occur at both the shear margin and near the grounding line when the ice front is retreated to the ridge crest. Should this increase in ~~flux out of the shelf (increase in melting)~~ be larger than the resulting increase in ~~flux to the shelf that results from ice sheet speed up~~ (from buttressing losses after calving), the ice shelf mass balance will reduce: calving will promote further ice shelf loss. However, these feedback arguments are qualitative; investigating the detailed response of the ice shelf mass balance after a calving event requires the use of a coupled ice-ocean model, and is beyond the scope of this study. (Here, we

true, unless calving fluxes subsequently reduce because more ice is taken away by melting.
 Ultimately $MB = q_{GL}(t) + q_{melt}(t) + q_{calving}(t)$

mass loss due to melting

across the grounding line

636 concerned ourselves only with the immediate melt response to calving, rather than the
 637 subsequent ice dynamic response.)

638 The magnitude of changes in melting with calving in our realistic simulations are
 639 similar to corresponding idealized simulations for the southern section of the cavity (i.e.
 640 very small), for which the offshore ridge-seabed gap is wide. However, for the northern
 641 section of the cavity (narrow ridge-seabed gap), the magnitude of changes are smaller
 642 than our idealized simulations predict. We attribute this difference to the complexities
 643 of the ice draft and seabed in the realistic simulations, and as well as our splitting of the
 644 inner cavity into two subsections. Splitting the cavity into two relies on the assumption
 645 that they are entirely dynamically disconnected. Although a strong PV barrier exists be-
 646 tween them, some flow is able to cross this barrier, providing a connection between the
 647 two regions. This inner cavity decomposition is also a convenient tool to allow us to cap-
 648 ture some of the effect of the inhomogeneity in ridge-draft gap along its length, but fur-
 649 ther work is required to fully understand the role of this inhomogeneity in controlling
 650 warm water access to the inner cavity. In addition, the sensitivity to cavity geometry
 651 means that the observed response may in fact be somewhat different to that predicted
 652 here: if, for example, uncertainties in the seabed bathymetry and/or ice shelf draft mean
 653 that the gap is smaller than used in our realistic simulation, the melt response to calv-
 654 ing might be significantly larger. In addition, the ice draft is not static but varies dy-
 655 namically; advection of thicker (thinner, respectively) sections of the ice shelf to the ridge
 656 crest will narrow (widen) the ridge-draft gap and thus increase (decrease) the sensitiv-
 657 ity of melt rates to calving.

658 The results presented in this paper have implications for melt rate parametriza-
 659 tions. At present, no melt rate parametrization is able to account for the position of the
 660 ice front, seabed topography, or any PV barrier when computing the melt rate (Assay-
 661 Davis et al., 2017). Although the example of PIG is somewhat extreme in this sense, we
 662 have demonstrated that the combination of seabed ridge and ice front position, which
 663 ultimately act as PV barriers, can be an important control on the melt rate applied to
 664 an ice shelf. This provides motivation for improvements in melt rate parametrizations.

665 It is important to note that MITgcm has a plethora of parameter choices and nu-
 666 matical settings, which might have an impact on the results of the simulations. These
 667 include choices of grid resolution, which are 400 m in the horizontal (to ensure mesoscale
 668 eddies are well resolved) and 10 m in the vertical. Simulations at higher vertical reso-
 669 lution (5 m) did not change the results significantly, although results were somewhat dif-
 670 ferent for lower resolution (20 m); this is perhaps unsurprising given that exchange over
 671 the ridge crest, which we have shown to be important in controlling the inner cavity melt
 672 rate, is expected to be highly sensitive to vertical resolution. Agreement with the higher
 673 resolution simulations gives us confidence that the simulations presented here are ap-
 674 propriately resolving exchange processes over the ridge crest.

675 Finally, it is important to note that forcing in our simulations comes exclusively
 676 from buoyancy fluxes and restoring at the boundaries. In particular, the simulations do
 677 not include either surface heat fluxes nor sea ice, which would be expected to alter the
 678 horizontal density gradients and thus circulation in the open ocean. In addition, they
 679 do not include wind stresses, which provide a leading order control on circulation in Pine
 680 Island Bay (Dutrieux et al., 2014).

681 8 Summary

682 The central aim of this study is to understand how, and why, melt rates on Pine
 683 Island Ice Shelf might respond to calving events that have already taken place, and those
 684 that might occur in future. We suggested at the outset that such calving events might
 685 relax the topographic barrier that currently restricts the access of warm water access to

the

-25-

Can you include a discussion on variations in P , which dominate the ocean variability in this region. Do results from idealized simul. hold in the realistic case? (see e.g. Dutrieux 2014), How do variations in P compare to variations in W for a range of l_c etc. E.g. $\#$ in becomes less sensitive to P for $l_c > 35$ etc.

686 the cavity inshore of the ridge. We have used numerical simulations in both an idealized
 687 domain, and one that is representative of PIIS, to address this question.

688 The idealized domain allowed us to isolate parametric dependence in the melt re-
 689 sponse to calving, and elucidate the mechanisms responsible for this response. We iden-
 690 tified a sensitive dependence on the cavity geometry via the parameter W that describes
 691 the gap between the seabed ridge and the ice base: configurations with a narrow gap ($W \lesssim$
 692 150 m) have a large response to calving, whereas those with wide gaps ($W > 150$ m) do
 693 not. For cavities with narrow gaps, we saw that: (1) the inner cavity melt rate does not
 694 change significantly with ice front retreat while the ice front is located some way (more
 695 than 20 km) offshore of the ridge, (2) as the ice front is retreated towards the ridge, the
 696 inner cavity melt rate increases significantly, before (3) dropping off sharply when the
 697 ice front is retreated to sit on top of the ridge if the pycnocline is relatively high or (4)
 698 increasing further if the pycnocline is relatively deep. In contrast, for configurations with
 699 wide gaps, the melt rate is largely independent of the location of the ice front. We de-
 700 scribed the roles of thermal driving and boundary layer velocity in these results, and elu-
 701 cidated the role of heat access to (and resulting stratification of) the inner cavity in this
 702 response. In particular, we saw that increased heat access to the inner cavity may, para-
 703 doxically, reduce inner cavity melt rates when it results in reduced stratification and thus
 704 a deceleration of the cavity circulation. Although these idealized results are intended to
 705 inform our understanding of melt rate changes beneath Pine Island Glacier, they can also
 706 be considered to be an archetype for situations in which seabed geometry obscures ac-
 707 cess of warm water to the grounding line of an ice sheet. This situation might be real-
 708 ized, for example, in ice sheet retreat over an over-deepened bed. In addition, the re-
 709 sults for wide gaps suggest that melt rates are insensitive to ice front position in cavi-
 710 ties with no seabed ridge.

711 The idealized experiments informed simulations performed using a cavity geom-
 712 etry that closely resembles PIIS, designed to assess how melt rates on PIIS might respond
 713 to calving in practice. This geometry has two inner cavity regions, which are approxi-
 714 mately dynamically disconnected. One of the inner cavity sections sits inshore of a nar-
 715 row section of the ridge-draft gap; in this region the melt rate increases with calving while
 716 the ice front is located offshore of the ridge, before reducing with further calving beyond
 717 the ridge. In contrast, the other sits inshore of a wide section of the ridge-draft gap; there
 718 the melt rate is largely independent of calving. Both of these observations are consis-
 719 tent with the idealized simulations, and the role of heat access to the inner cavity

720 Our results suggest that PIIS sits in a small safety band: melt rates in dynamically
 721 important regions will not change significantly until the ice front retreats closer to the
 722 ridge. This lack of melt rate response while the ice sheet accelerates in response to a loss
 723 of buttressing acts as a negative feedback, promoting regrowth of the shelf. However, if
 724 calving maintains its current pace, large increases in melt rates in these dynamically im-
 725 portant regions will be realized sometime in the next decade or so. This increase in melt
 726 has the potential to act as a positive feedback in which the melt response to calving leads
 727 to further ~~disintegration~~ of the ice shelf. In addition, the sensitivity to cavity geometry
 728 identified in the idealized results, and uncertainty (or dynamic changes in) the cavity ge-
 729 ometry mean that the observed response may be significantly larger than predicted here.

thinning & weakening

Acknowledgments

Enter acknowledgments, including your data availability statement, here.

References

- Arthern, R. J., & Williams, C. R. (2017). The sensitivity of west antarctica to the
 submarine melting feedback. *Geophys. Res. Lett.*, 44(5), 2352–2359.